# Linear instability mechanisms leading to optimally efficient locomotion with flexible propulsors

K. W. Moored, P. A. Dewey, B. M. Boschitsch, A. J. Smits, and H. Haj-Hariri

Citation: Physics of Fluids (1994-present) **26**, 041905 (2014); doi: 10.1063/1.4872221
View online: http://dx.doi.org/10.1063/1.4872221
View Table of Contents: http://scitation.aip.org/content/aip/journal/pof2/26/4?ver=pdfcov
Published by the AIP Publishing

PHYSICS OF FLUIDS **26**, 041905 (2014)

# Linear instability mechanisms leading to optimally efficient locomotion with flexible propulsors

K. W. Moored,[1,a)] P. A. Dewey,[2] B. M. Boschitsch,[2] A. J. Smits,[2,3] and H. Haj-Hariri[4]
[1]*Mechanical Engineering and Mechanics, Lehigh University, Bethlehem, Pennsylvania 18015, USA*
[2]*Department of Mechanical and Aerospace Engineering, Princeton University, Princeton, New Jersey 08544, USA*
[3]*Department of Mechanical and Aerospace Engineering, Monash University, VIC 3800, Australia*
[4]*Department of Mechanical and Aerospace Engineering, University of Virginia, Charlottesville, Virginia 22904, USA*

(Received 10 May 2013; accepted 9 April 2014; published online 29 April 2014)

We present the linear stability analysis of experimental measurements obtained from unsteady flexible pitching panels. The analysis establishes the connections among the wake dynamics, propulsor dynamics, and Froude efficiency in flexible unsteady propulsion systems. Efficiency is calculated from direct thrust and power measurements and wake flowfields are obtained using particle image velocimetry. It is found that for flexible propulsors every peak in efficiency occurs when the driving frequency of motion is tuned to a wake resonant frequency, not a structural resonant frequency. Also, there exists an optimal flexibility that globally maximizes the efficiency. The optimal flexibility is the one where a structural resonant frequency is tuned to a wake resonant frequency. The optimally tuned flexible panels demonstrate an efficiency enhancement of 122%–133% as compared to an equivalent rigid panel and there is a broad spectrum of wake resonant frequencies allowing high efficiency swimming over a wide range of operating conditions. At a wake resonant frequency we find that the entrainment of momentum into the time-averaged velocity jet is maximized.
 [http://dx.doi.org/10.1063/1.4872221]

## I. INTRODUCTION

Here we analyze new experimental results on the flow fields produced by flexible propulsors in terms of a linear stability analysis on the mean flow in the wake. The analysis is then substantiated using thrust and efficiency performance data obtained previously for the same flexible propulsors.[1]

The vortex wakes produced by swimming animals and pitching panels alike are formed by the wrapping of shed vorticity into discrete vortex cores. This process is nonlinear, but the mean flow is well-defined and a linear stability analysis can give considerable insight on the wake formation. For example, Barkley[2] and Thiria and Wesfreid[3] show that the time-averaged velocity field behind stationary cylinders producing a von Kármán vortex street is the steady solution to the forced Navier-Stokes equations so that it is amenable to a linear stability analysis. Similarly, linear stability analysis of the time-averaged flow has been applied to turbulent pipe flow to find the most amplified velocity response.[4]

In the context of oscillating propulsors, a variety of different wakes can form,[5–7] but they all induce a wavy and unsteady velocity jet that imparts momentum to the fluid. Triantafyllou *et al.*[8,9] showed that the time-averaged velocity jet is convectively unstable and that there is a "preferred" frequency at which the von Kármán instability was the most unstable. They further suggested that a

a)kmoored@lehigh.edu

 

single peak in efficiency was attained by tuning the driving frequency of motion to the frequency of maximum spatial growth (the "preferred" frequency) of the velocity jet in a two-dimensional flow.

Moored *et al.*[10] generalized this approach by introducing wake resonance theory, which supposes that there may exist multiple frequencies at which the jets are maximally unstable. When the driving frequency of a system is tuned to the most unstable frequency of its jet, however, it is expected that a local peak in efficiency occurs. The specific frequency where the driving and the most unstable frequency of the jet are aligned is called the wake resonant frequency. Also, the structure of some vortex wakes changes when the instability mode of the jet at the driving frequency transitions to a new instability mode. Moored *et al.* corroborated these elements of the theory by performing experiments on an oscillating three-dimensional bio-inspired fin, which were analyzed without considering its passive flexibility.

To extend wake resonance theory to unsteady flexible systems, which is the subject of the present work, we postulate that in flexible systems the peaks in efficiency also occur at wake resonant frequencies. That is, there are two important characteristic frequencies in flexible unsteady propulsion: the structural resonant frequency and the wake resonant frequency. We therefore propose that when the structural resonant frequency is tuned to a wake resonant frequency, the efficiency performance will show an improvement. This postulate implies that operating at structural resonance alone does not necessarily lead to a local peak in efficiency, and may help to explain some of the divergent results obtained in previous studies. For instance, Vanella *et al.*[11] numerically investigated a two-dimensional, discretely flexible two-link propulsor to find that peak efficiency occurred at $f_1^* = 0.33$, where $f_n^* = f/f_n$, so that $f$ is the driving frequency and $f_n$ is the $n$th structural resonant frequency of the fluid-propulsor system. In contrast, the optimal efficiency of flexible propulsors has been found to occur at $f_1^* = 0.4$,[12] $f_1^* = 0.35$–$0.5$,[13] and $f_1^* = 0.7$,[14] using scaling arguments, two-dimensional computations, and three-dimensional experiments, respectively. Michelin *et al.*[15] found that for inviscid two-dimensional flow the efficiency had a maximum at $f_2^* = 1$, while for free swimming conditions Spagnolie *et al.*[16] and Alben *et al.*[17] showed that optimal conditions occurred at $f_1^* \approx 1$ for both experiments and computations. Finally, Masoud *et al.*[18] found that the peak efficiency appeared at $f_1^* = 1.2$–$1.3$ for a three-dimensional wing at a net angle of attack, while Dai *et al.*[19] found a peak efficiency at $f_1^* > 1$ for a flexible pitching panel of finite aspect ratio.

Here, we present new experiments on nominally two-dimensional pitching panels with various degrees of flexibility, and we demonstrate that the optimally efficient performance occurs for the cases where the structural resonance is tuned to a wake resonance, thereby extending wake resonance theory to flexible systems. By considering the entrainment of momentum into the time-averaged jet, we provide further physical insights in wake resonance theory.

## II. EXPERIMENTAL METHODS

The experimental arrangements are the same as those used by Dewey *et al.*,[1] where further details regarding the experimental apparatus and procedures may be found. Water channel experiments were conducted using rectangular panels having a chord length $C = 120$ mm and a span of 280 mm. The panels spanned the entire depth of the water channel to minimize the three-dimensional effects of the flow. The panels were attached to a pitching shaft at their leading edge that was harmonically oscillated by a HiTec HS 7940-TH servo motor. The chord length was selected to achieve a Reynolds number of $7200 \pm 2\%$, which is biologically relevant,[20] at a flow velocity $U_\infty = 0.06$ m/s. In total, seven panel stiffnesses were considered, where the stiffness was controlled by altering the panel thickness, $h$. Thin plates were selected in favor of hydrofoils to act as a simplified model of fish fins as has previously been used by Green *et al.*[21] and Lauder *et al.*[22] Additionally, the flexural rigidity ($EI$, where $E$ is the modulus of elasticity and $I$ is the area moment of inertia) of the panels ranged from $4.2 \times 10^{-4}$–$1.1 \times 10^{-2}$ Nm$^2$, which matches well with the flexural rigidity of biological propulsors studied by Lauder *et al.*[22] For the effectively rigid panel, a 3 mm thick acrylic panel was used. We will refer to the panels as $P_\infty$ for the rigid panel, and $P_1$ to $P_6$ for the flexible panels, where subscripts 1 and 6 represent the most and least flexible panels, respectively.

The characteristic non-dimensional properties of the panels are given in Table I. As per Kang *et al.*,[12] the non-dimensional effective stiffness is $\Pi_1 = Eh^{*3}/\left[12(1-\nu_s^2)\rho_f U_\infty^2\right]$, where $h^* = h/C$,

TABLE I. Physical properties of flexible panels. Superscript *a* indicates estimated value.

| Panel | $P_1$ | $P_2$ | $P_3$ | $P_4$ | $P_5$ | $P_6$ | $P_\infty$ |
|---|---|---|---|---|---|---|---|
| $\Pi_1$ | 0.3 | 0.7 | 1.4 | 2.0 | 4.0 | 7.8 | $\mathcal{O}(10^4)$ |
| $h^*(\times 10^{-3})$ | 1.1 | 1.6 | 2.1 | 3.2 | 4.2 | 5.3 | 26.5 |
| $k_1$ | 1.3[a] | 2.3[a] | 6.3 | 6.9 | 9.4 | 12.6 | |

$\nu_s$ is Poisson's ratio and $\rho_f$ is the density of the fluid. The non-dimensional effective stiffness is also the inverse of a Cauchy number.[23] Here, $k_1 = 2\pi f_1 C/U$ is the reduced frequency at the first structural resonant frequency where the length scale is based on the chord. The density ratio for each panel is $\rho^* = 1.3$, where $\rho^* = \rho_s/\rho_f$ and $\rho_s$ is the density of the panel. Altogether, 27 evenly spaced reduced frequencies ($k = 2\pi fC/U$), ranging from $k = 2.5$–18.8, were considered for each panel. For all cases examined, the maximum pitching angle of the leading edge, $\theta_0$, was held constant, and chosen such that the peak-to-peak amplitude of the trailing edge motion for the rigid panel was $A_\infty = 0.25\,C$. The amplitude of the trailing motion for the flexible panels, $A$, depends upon the passive response of the panel and it is $A$ that is used to define the Strouhal number, $St = fA/U$.

The analysis will be based on the wake mean velocity profiles. These profiles were measured using particle image velocimetry (PIV), and they are presented here for the first time. The PIV system consisted of a Coherent Innova 70C continuous wave argon-ion laser as the light source, a Redlake MotionXtra HG-LE CCD camera with 1128 × 752 pixel resolution for the imaging, and neutrally buoyant silver coated hollow ceramic spheres with a mean diameter of 93 $\mu$m for the particle seeding (Potters Industries Inc. Conduct-O-Fil AGSL150 TRD).

PIV measurements were taken for all seven panel stiffnesses at a range of reduced frequencies from $k = 1.25$–12.5, resulting in a total of 72 separate cases. The oscillation period of the pitching panel was discretized into 25 phases by the LabView code controlling the system, and at each of these 25 phases a timing-control system (Stanford Research System DG535) triggered the camera to take a pair of images at a frequency of 80 Hz. Data were acquired for 24 oscillation periods resulting in 600 image pairs. Two-dimensional velocity fields were computed by calculating local spatial cross-correlations over two passes, with window sizes of 64 × 64 and 32 × 32 pixel windows with 50% overlap.[24] The resulting vectors were spaced 16 pixels apart for a spatial resolution over the interrogation region of roughly 30 velocity vectors per chord length. Earlier tests[25,26] indicate errors in velocity to be approximately 1%–5%.

## III. PROPULSIVE EFFICIENCY

The Froude efficiency $\eta$ is defined as the ratio of the useful power output to the power input to the fluid, $\mathcal{P}$, where the useful power output is the product of the time-averaged thrust $T$ and the swimming speed $U_\infty$, such that $\eta = TU_\infty/\mathcal{P}$. Dewey *et al.*[1] presented thrust, power and efficiency measurements in the same apparatus for nominally two-dimensional pitching panels, as well as pitching panels of finite aspect ratio, and found that flexible panels can give a significant amplification of thrust production of $\mathcal{O}$(100%–200%) and propulsive efficiency of $\mathcal{O}$(100%) when compared to rigid panels. We will use the propulsive efficiency results reported by Dewey *et al.*, shown in Figure 1, for the current analysis. Two of the major findings of Dewey *et al.* that are addressed in the current effort are (1) that there was an optimal flexibility that maximizes efficiency (Figure 1(c)), and (2) the peaks in propulsive efficiency could occur below, at, or above the resonant frequency of the panel depending on the panel flexibility (Figure 1(d)).

## IV. EXPERIMENTAL RESULTS

The spanwise vorticity fields acquired using PIV at the most efficient case ($P_3$, $k = 6.3$) are shown in Figure 2. The evolution of the wake is shown for the first half of the oscillation period, $T_p$. At the start of the period, a shear layer is shed into the wake (Figure 2(a)). The shear layer rolls

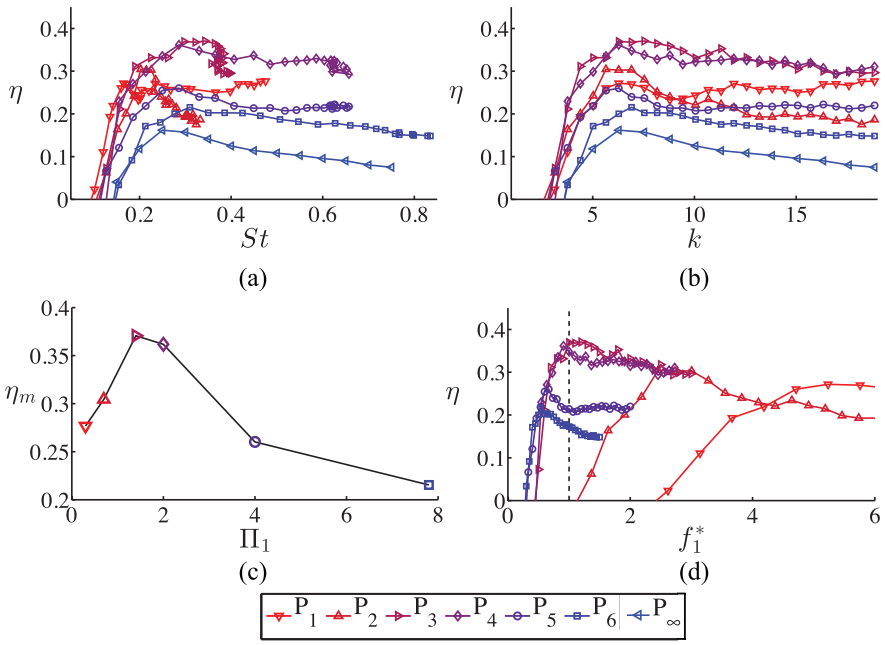


FIG. 1. (a) Efficiency as a function of Strouhal number. (b) Efficiency as a function of reduced frequency. (c) Maximum efficiency, $\eta_m$, as a function of effective panel stiffness. (d) Efficiency as a function of reduced natural frequency. The peak efficiencies fall into three regimes: (1) $f_1^* < 1$, (2) $f_1^* = 1$, and (3) $f_1^* > 1$. (a) and (b) Reprinted with permission from P. A. Dewey, B. M. Boschitsch, K. W. Moored, H. A. Stone, and A. J. Smits, "Scaling laws for the thrust production of flexible pitching panels," J. Fluid Mech. **732**, 29–46 (2013). Copyright 2013 Cambridge University Press.

up, and the vortex core propagates downstream, while still being connected to the trailing edge of the panel by an extended shear layer (Figure 2(b)). As the pitching panel reverses its direction ($T_p = 0.25$), the sign of the shear layer changes, and another vortex roll-up will occur so that a second vortex of opposite sign is shed into the wake, as in Figure 2(c). The vortices align themselves into a reverse von Kármán vortex street, and the induced velocity between subsequent vortices will have a component in the streamwise direction indicating momentum addition to the fluid and a net thrust.

Time-averaged velocity profiles can be extracted by time-averaging the measured wakes of the panels. Figure 3 shows the time-averaged velocity profiles at a location $C/3$ downstream from the trailing edge for all panels at a frequency of $k = 7.5$. At this intermediate frequency, the most flexible panel, $P_1$, produces a velocity profile depicting a jet of fluid containing the least amount of momentum. The peak jet velocity contained in the profile continues to increase with increasing

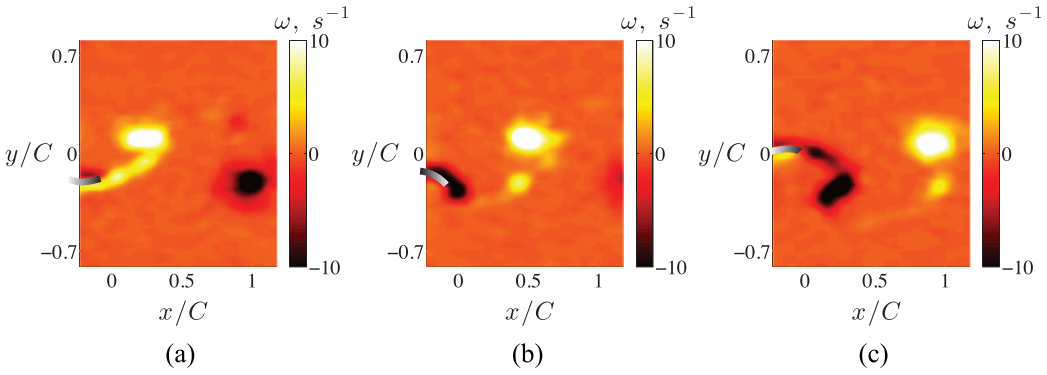


FIG. 2. Evolution of the vorticity field in the wake of panel $P_3$ near the optimal efficiency case ($k = 5.7$, $f^* = 0.9$). (a) $t/T_p = 0$, (b) $t/T_p = 0.25$, (c) $t/T_p = 0.5$. Flow is from left to right; approximate location of panel is outlined with the curved line.

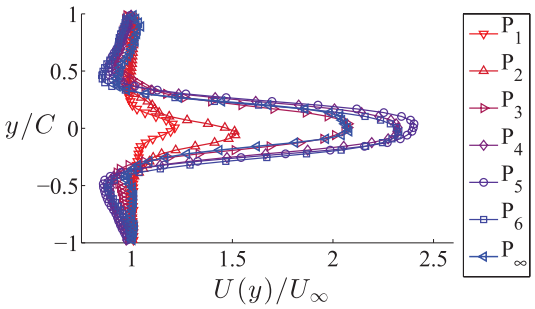


FIG. 3. Time-averaged velocity profiles for $k = 7.5$ extracted at a location $C/3$ downstream of the trailing edge of the panels.

stiffness until a maximum peak velocity is obtained for panel $P_5$. A further increase in stiffness, as for panel $P_6$ and the rigid panel $P_\infty$, yields a decrease in the peak velocity.

## V. LINEAR STABILITY ANALYSIS OF VORTEX WAKES

The process that generates the vortex wake flow downstream of an unsteady propulsor is a nonlinear one. However the mean flow is well-defined and its stability can be analyzed via a linear analysis, as shown by Barkley[2] and Thiria and Wesfreid[3] in the context of the nonlinear von Kármán vortex street behind a cylinder in uniform flow. Here we will closely follow the approach of Barkley[2] in analyzing the wake formed by flexible, pitching panels.

Consider a reverse von Kármán vortex street in the wake of a pitching panel, a periodic flow. The two-dimensional flow field can be decomposed into its respective time-averaged field and time-varying fluctuation without loss of generality, so that

$$\mathbf{u}(x, y, t) = \bar{\mathbf{u}}(x, y) + \mathbf{u}'(x, y, t),$$
$$P(x, y, t) = \bar{P}(x, y) + P'(x, y, t),$$

where

$$\bar{\mathbf{u}}(x, y) = \frac{1}{T}\int_0^T \mathbf{u}(x, y, t)\, dt,$$
$$\bar{P}(x, y) = \frac{1}{T}\int_0^T P(x, y, t)\, dt.$$

Here, $\mathbf{u}$ is the velocity vector in the plane $[x, y]$, $P$ is the pressure, overbars denote time-averaged quantities, and primes denote fluctuations. The period of vortex shedding is $T$. If the decomposition is substituted into the Navier-Stokes and continuity equations and then time-averaged, the classical time-averaged governing equations are developed:

$$(\bar{\mathbf{u}} \cdot \nabla)\bar{\mathbf{u}} = -\nabla \bar{P} + \frac{1}{Re}\nabla^2 \bar{\mathbf{u}} - \frac{1}{T}\int_0^T (\mathbf{u}' \cdot \nabla)\mathbf{u}'\, dt, \tag{1}$$

$$\nabla \cdot \bar{\mathbf{u}} = 0. \tag{2}$$

The far right term of Eq. (1) captures the effect of Reynolds stresses on the time-averaged flow, where the stresses are associated with the vortex shedding. Now consider the forced Navier-Stokes equation where the forcing $\mathbf{F}$ is due to vortex shedding from the pitching propulsor. That is,

$$\frac{\partial \mathbf{u}}{\partial t} + (\mathbf{u} \cdot \nabla)\mathbf{u} = -\nabla P + \frac{1}{Re}\nabla^2 \mathbf{u} + \mathbf{F}. \tag{3}$$

It is clear that the time-averaged fields satisfy the forced Navier-Stokes equation and therefore they are amenable to a linear stability analysis. The time-averaged jet structures behind flapping foils are only weakly nonparallel and of the convective type so that we use a spatial stability analysis.[27]

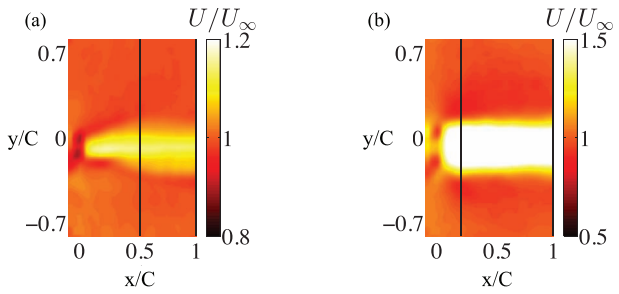


FIG. 4. Example time-averaged velocity fields for (a) panel $P_1$ and (b) panel $P_6$ at the reduced frequency, $k = 6.3$. The solid lines show the downstream range where velocity profiles were extracted for the linear spatial stability analysis. For panel $P_1$ this range is $0.5 \leq x/C \leq 1$ while for the other panels the range is $0.2 \leq x/C \leq 1$.

To explore the connection between the efficiency measurements and the mean flow data, we now apply wake resonance theory as described by Moored *et al.*[10] First, a linear spatial stability analysis is performed on the time-averaged flow field, which is taken to be locally parallel (Figures 4(a) and 4(b)). A one-dimensional velocity profile, $\mathbf{U} = [U(y),\ 0]$, is then extracted (Figure 3) from a downstream location of the time-averaged velocity field and used in the analysis, which in the case of the forced Navier-Stokes equations is the time-averaged flow. A small perturbation, $\mathbf{u} = [u,\ v]$, is superimposed onto the base flow and substituted into the forced Navier-Stokes and continuity equations. The equations are then linearized about the base flow and a traveling wave form of the solution is assumed for the velocity perturbations, or equivalently, for the stream function perturbations. Following Barkley,[2] the Reynolds stresses are assumed to be unperturbed, which presents a limitation of the present method.

The linearization results in the classic Orr-Sommerfeld equation for the complex amplitude, $\phi(y)$, of the wave-like perturbation to the stream function, $\psi(x, y, t)$, given by (with $D \equiv d/dy$)

$$\left\{\left(D^2 - \alpha^2\right)^2 - i\ Re\left[(\alpha U - k)\left(D^2 - \alpha^2\right) - \alpha U''\right]\right\}\phi = 0, \tag{4}$$

where

$$\psi(x, y, t) = \phi(y)\, e^{i(\alpha x - kt)} \equiv \phi(y)E. \tag{5}$$

All parameters and variables are nondimensionalized using the characteristic length and velocity scales $C$ and $U_\infty$. The complex wavenumber is $\alpha = k/c$ where $c$ is the complex phase velocity and $k$ is the reduced frequency. The Reynolds number is $Re = \rho_f U_\infty C/\mu$, where $\rho_f$ and $\mu$ are the fluid density and dynamic viscosity, respectively.

For a spatial stability analysis the wavenumber is complex ($\alpha = \alpha_r + i\,\alpha_i$) and the reduced frequency is real. When $\alpha_i$ is negative and $x > 0$ (downstream of the perturbations), the stream function and velocity perturbations will grow in space. In an unbounded domain, the boundary conditions ensure decay of the perturbations and their spatial derivative far away from the centerline of a jet.

To solve the nonlinear eigenvalue problem, the Orr-Sommerfeld equation is expanded in powers of $\alpha$ and then discretized over $y \in [-Y, Y]$, along with the boundary conditions, for some large value of $Y$. The discretized nonlinear eigenvalue problem is then cast into the companion matrix form,[28–30] which produces a linear eigenvalue problem that can be solved using standard techniques. In the analysis of the experimental data, 250 discretization points were used for the computations. Doubling the discretization to 500 points caused a change of less than 1% of the real and imaginary parts of the eigenvalues. The canonical problem of plane Poiseuille flow[31] was used to validate the numerics.[10]

Each velocity profile was discretized into 250 points and the stability analysis was conducted for 50 real perturbation frequencies, $k$, ranging from $0.5 < k < 17$. The most unstable eigenvalue, $\alpha_i$, for each perturbation frequency was compiled to form a stability curve for that velocity profile (see Moored *et al.*[10]). For each stability curve there is a driving frequency at which the velocity profile was physically generated and the most unstable frequency where the velocity profile is maximally

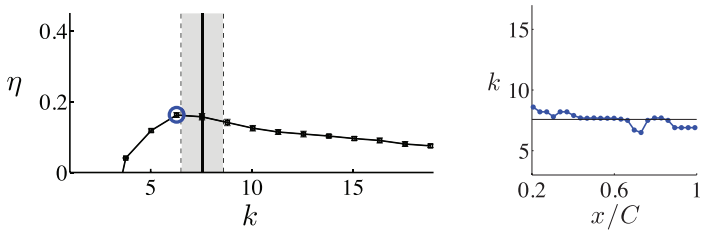


FIG. 5. Rigid panel (left) efficiency data and (right) wake resonant frequencies as a function of downstream location. The circle on the efficiency data marks the efficiency peak. The solid vertical lines denote the mean values of the wake resonant frequency, the dashed lines represent the uncertainty.

unstable. If the driving frequency is tuned to the most unstable frequency of the velocity jet then that frequency is termed a wake resonant frequency. This tuning process is nonlinear as the most unstable frequency is a nonlinear function of the driving frequency.

To determine the resonance condition precisely can be laborious in cases where the stability curves are sensitive to small changes in the driving frequency. Instead, a relaxed condition is applied where the propulsor is said to "resonate" with the wake instability when the spatial growth rate, $\alpha_i$, at the driving frequency is within 5% of the maximum spatial growth rate (occurring at the most unstable frequency).

At resonance the perturbations experience their maximum amplification, and can act to enhance entrainment of momentum into the velocity jet. We show in Sec. VII that the entrainment of momentum near the trailing-edge of the propulsor is maximized at a wake resonance, thereby enhancing the momentum flux and leading to higher efficiency. Thus a peak in the propulsive efficiency is expected when the fin is driven at a wake resonant frequency. This argument is similar to that used to describe optimal vortex formation from the viewpoint of the formation time,[32] although the connection between wake resonance and formation time has yet to be established.

The estimates of the wake resonant frequencies are subject to uncertainties in the PIV measurements, and to the choice of downstream location. From a 1%–5% uncertainty in the velocity measurements the estimated uncertainty in the calculation of the wake resonant frequencies is 1%–3.5% (see the Appendix). For $0.2 < x/C < 1$, the locally parallel flow assumption holds for all of the jet structures produced by the panels except for the most flexible panel where the assumption holds for $0.5 < x/C < 1$. Locally parallel flow occurs when the velocity jet width, $\delta(x)$, changes slowly over a typical instability wavelength, that is, $\epsilon = [\lambda_{tip}/\delta(x)](d\delta/dx) \ll 1$.[33] In our case, we use the condition that $\epsilon < 0.5$. The most flexible panel has a value of $\epsilon = 1.19$ in the range $0.2 < x/C < 0.5$ for some of the frequencies leading to the omission of this range from the analysis.

Thirty-two downstream stations for each panel were examined within the prescribed range at every frequency that PIV data was acquired. At each downstream location where a wake resonance condition was met, that frequency was marked as a blue point in Figures 5 and 6 (right). The mean values of the wake resonant frequencies within that range are the solid horizontal lines in Figures 5 and 6 (right) while they are represented by the solid vertical lines in Figures 5 and 6 (left). The minimum and maximum values of the wake resonant frequencies within the downstream range are denoted by the grey regions bounded by dashed lines in Figures 5 and 6 (left). The grey regions reflect the uncertainty in the measurement of the wake resonant frequency. There is also a variance of 3%–15% in the full-scale measurement of efficiency marked by the error bars.

## VI. ANALYSIS OF THE EXPERIMENTAL DATA

Figure 5 presents the efficiency data and the wake resonant frequency as a function of the downstream location determined for the rigid pitching panel, where the structural resonant frequency is effectively at $f_1 = \infty$. For the rigid panel there is only a single wake resonant frequency detectable at every downstream location examined. Within the range of downstream values, the wake resonant

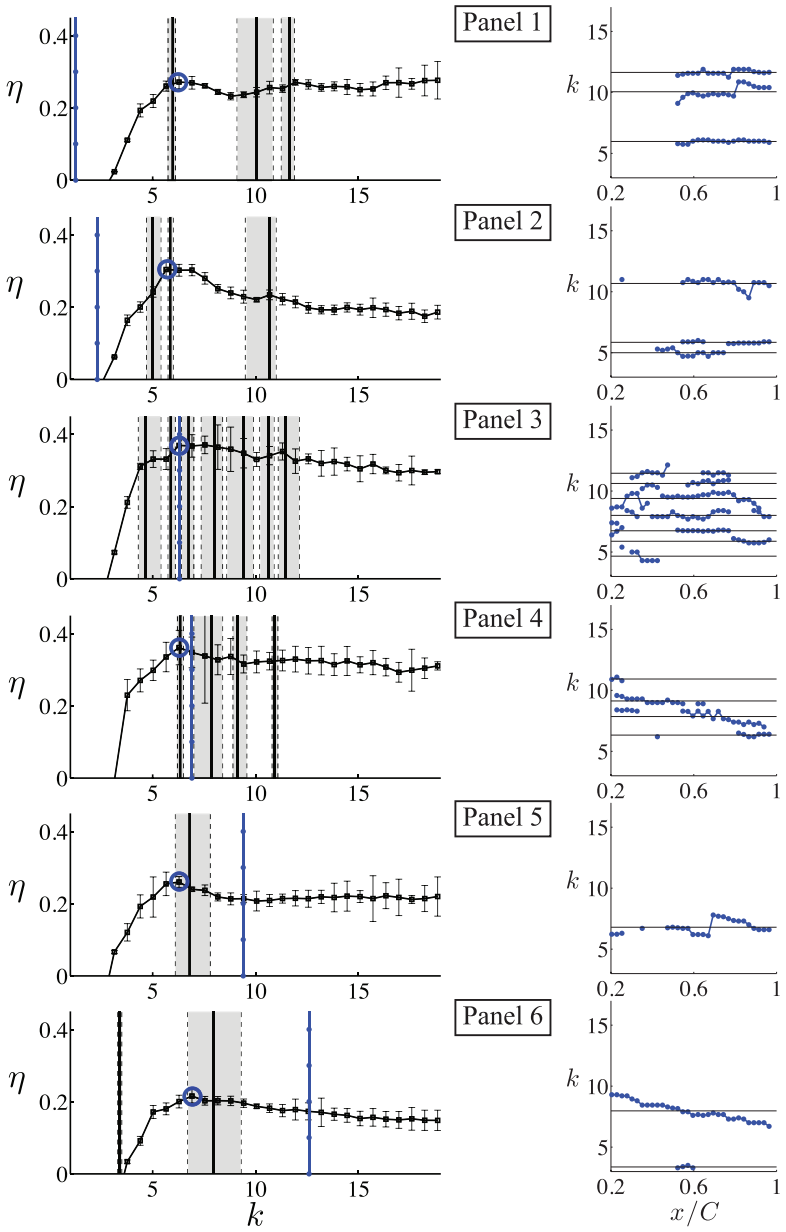


FIG. 6. Flexible panels (left) efficiency data and (right) wake resonant frequencies as a function of downstream location. The solid vertical lines denote the wake resonant frequencies, the dashed lines represent the uncertainty in the wake resonant frequencies and the dotted-solid vertical lines represent the structural resonant frequencies.

frequency aligns with the peak value of efficiency (Figure 5(a)) as expected,[10] which in this case is $\eta = 16\%$.

Figure 6 presents similar data for the flexible pitching panels. It is evident that for each flexible panel every primary peak in efficiency (marked by a circle) aligns with a wake resonant frequency (marked by a solid vertical line), within the stated uncertainty. Many of the secondary wake resonant frequencies may align with small local peaks that cannot be distinguished from the uncertainty in the efficiency measurements. Nevertheless, it can be seen that the most flexible cases (panels $P_1$ to $P_4$) have multiple wake resonant frequencies. Note also that panel $P_6$ has a wake resonant frequency for a drag production case. For the most efficient cases of panels $P_3$ and $P_4$, there are seven and four wake resonant frequencies detected, respectively. The wake resonant frequencies are distinguishable

since many of the them exist simultaneously at a given downstream location. For panel $P_3$, which represents the optimal flexibility, there is almost a continuum of wake resonant frequencies producing a large region of high efficiency. This has broad implications on unsteady swimming with flexible propulsors, in that at the optimal flexibility there exist numerous wake resonant frequencies so that high efficiency swimming is possible over a wide range of operating conditions.

In contrast to the wake resonant frequencies, the structural resonant frequencies only closely align with efficiency peaks in the cases of panels $P_3$ and $P_4$, where wake resonant frequencies *also* coincide with the efficiency peaks. For flexible propulsors, therefore, each peak in efficiency occurs when the driving frequency of motion is tuned to a wake resonant frequency, not to a structural resonant frequency.

The cases that lead to global optimally efficient locomotion are panels $P_3$ and $P_4$ that exhibit a 133% and 122% increase in efficiency ($\eta = 38\%$ and 36%), respectively, when compared to the rigid panel ($\eta = 16\%$). Here, the structural resonant frequencies of the panels are closely aligned with their wake resonant frequencies. When this special condition is satisfied, flexible panels will be described as "tuned" flexible panels. Conversely, when the special condition is not satisfied, flexible panels will be described as "untuned" flexible panels.

For the untuned flexible panels, there is still an efficiency enhancement over the rigid panel for every case examined in this study, of between 33%–88% ($\eta = 22\%$–30%). As the structural resonance frequency and a wake resonance frequency come closer together, the efficiency curves are amplified, which can be seen when comparing panels $P_1$–$P_3$ and panels $P_4$–$P_6$. There is no particular effect on the efficiency when operating at structural resonance alone as can be seen in the data for panels $P_5$ and $P_6$. For these panels the efficiency is effectively flat when operating near structural resonance and these frequencies are clearly not producing peak efficiency. The experimental data covers a range of cases where the optimal driving frequency is $f_1^* < 1$ (the rigid panel, panels $P_5$ and $P_6$), $f_1^* \approx 1$ (panels $P_3$ and $P_4$), and $f_1^* > 1$ (panels $P_1$ and $P_2$). This data set covers the entire range of the cases seen in previous work.[11–18] It seems clear that these divergent observations can be explained by the fact that the primary mechanism to achieve efficient locomotion is to tune the frequency of motion to a wake resonant frequency, while the secondary mechanism is to tune a structural resonant frequency to a wake resonant frequency.

The efficiency data along with the detected wake resonant frequencies are shown in Figure 7 as a function of Strouhal number. Here, the Strouhal number of the wake resonant frequencies and structural resonant frequencies are interpolated from the relationship between $k$ and $St$ for each panel. Note that the seven wake resonant frequencies of panel $P_3$ collapse to only four distinct frequencies in $St$ space. The wake resonant frequencies found in this study collectively cover a Strouhal range of $0.16 \leq St \leq 0.42$. All of the identified wake resonant frequencies from the literature[9,10,34] fall within the range of this study. When including this literature, the range is derived from two-dimensional computations and experiments as well as three-dimensional experiments with both rigid and flexible propulsors, and offers the most comprehensive range of optimal Strouhal number in the literature that is based on wake resonance principles. This range is close to the range of $0.2 \leq St \leq 0.4$ determined from statistical analysis of the Strouhal numbers exhibited by a collection of flying and swimming animals.[35] These ranges, however, must be used as only approximate estimates of an optimal $St$. For instance, Clark and Smits[36] observed efficiencies between $\eta = 35\%$–55% in the range $0.16 \leq St \leq 0.42$; an approximately 50% variation within the "optimal" range. Thus, operating a device or an animal within the optimal Strouhal range is an insufficient condition to determine whether it is tuned to the resonance of its wake and hence whether it attains locally efficient propulsion. Nevertheless, the alignment of the range of wake resonant frequencies and range of most flying and swimming animals, suggests a unifying principle in biological locomotion (at least at $Re \gg 1$), namely, that animals tune to the hydrodynamic resonance of their wakes regardless of whether their propulsors are rigid or flexible.

## VII. MOMENTUM ENTRAINMENT

We now examine the physical mechanism responsible for a peak in efficiency when operating at a wake resonant frequency. We propose that when a propulsor is driven at a wake resonant frequency

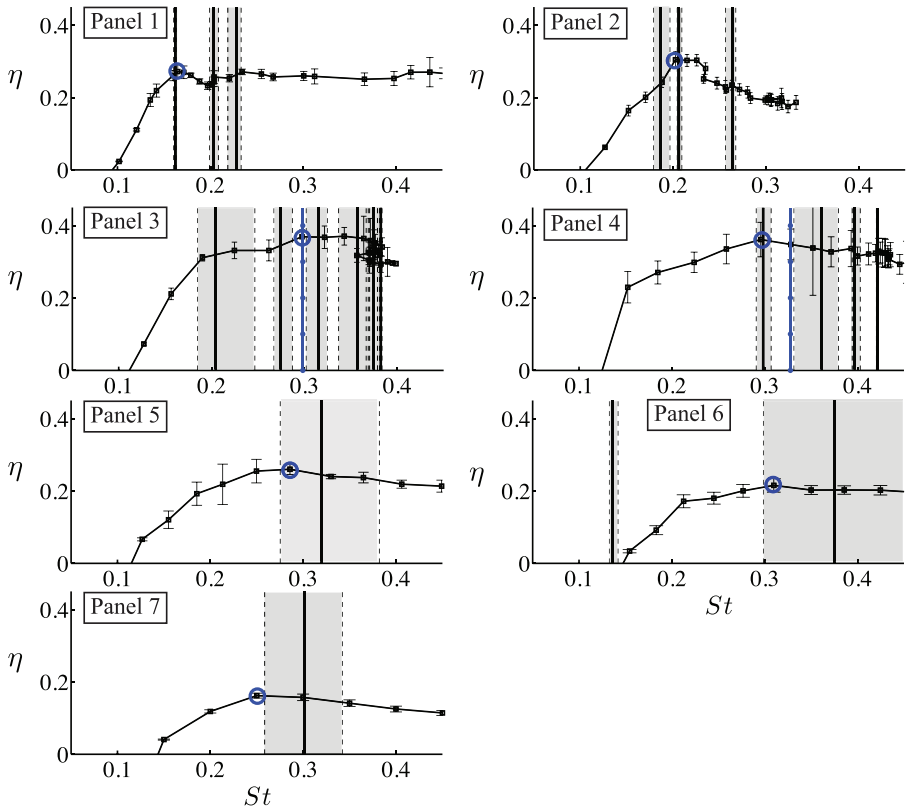


FIG. 7. All panels efficiency as a function of Strouhal number. The solid vertical lines denote the wake resonant frequencies, the grey regions represent the uncertainty in the wake resonant frequencies and the dotted-solid vertical lines represent the Strouhal number at which the structural resonant frequencies occur.

there is an increase in the entrainment of momentum into the time-averaged velocity jet. Importantly, the problem is semi-infinite, that is, the jet flow forms at the trailing-edge and extends to infinity. As such there is a formation region where shed vorticity is fed into rolling-up vortices. If an element of shed vorticity were to move downstream across the formation region at a constant speed, then in the time-average sense there would be no cross-stream velocity due to the canceling of the induced velocity from the element at different times (assuming low diffusive losses over the time interval of transit). However, in this region the stream-wise advection of the feeding shear layer vorticity is faster than the stream-wise advection of the forming vortex cores, hence the concentration of vorticity into cores. The stream-wise advection of an element of vorticity then slows down. This leads to a non-zero time-averaged cross-stream velocity when an element of vorticity resides in the downstream portion of the formation region for a longer period of time. Thus, over a finite region behind the trailing-edge entrainment occurs (Figure 8(b)). As shown in Moored *et al.*[10] (see Figure 9) the mean flow superposed with the most unstable linear waves produces a perturbed vorticity pattern with regions of stream-wise vorticity compression that will tend to accelerate vorticity into the forming vortex cores shed from the trailing-edge. Thus, when operating at a wake resonance we expect the time-averaged cross-stream velocity and the entrainment to be enhanced due to an expedited rollup. The most unstable linear perturbations accelerate the vorticity toward its final state, however, the rollup and entrainment processes are highly nonlinear. This is akin to the linear waves of a Kelvin-Helmholtz instability compressing and transversely displacing vorticity leading to the formation of vortices through a nonlinear Biot-Savart rollup.[37,38]

To examine this postulate, the PIV data is analyzed by using a control volume (CV) with its inlet located at the trailing-edge of the panel and its outlet is placed as far downstream as (positive) entrainment is occurring. The sides of the CV are centered symmetrically around the peak velocity

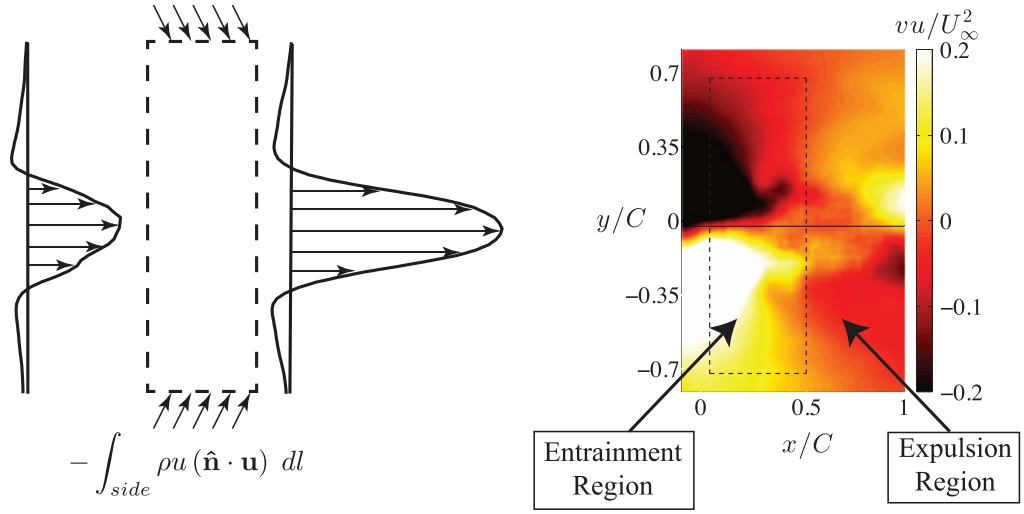


FIG. 8. Panel 5: $k = 6.9$ (Left) Schematic of the CV with the measured inlet and outlet profiles. Momentum is being entrained through the sides of the CV to enhance the momentum of the velocity profile at the outlet. (Right) The product of the instantaneous velocities $u$ and $v$, showing where momentum is entrained into or expelled from the velocity jet.

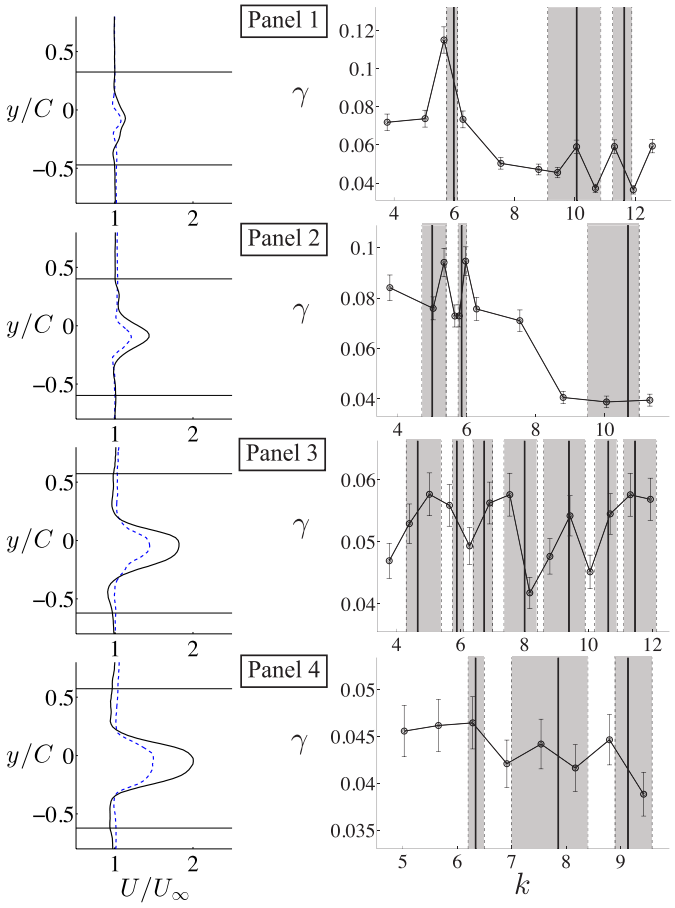


FIG. 9. Data for the most flexible panels $P_1$–$P_4$: (Left) Velocity profiles at $k = 6.3$ for the inlet (dashed profile) and the outlet (solid profile). The sides of the CV are marked with horizontal solid lines. (Right) Entrainment ratio as a function of reduced frequency. The solid line represents the mean values of the wake resonant frequencies while the dashed lines are the minimum and maximum values of the wake resonant frequencies.

at the inlet at a location where the velocity has recovered to within 2% of the peak velocity of the jet. The side locations of the CV are fixed for a given panel over the range of tested frequencies for the frequency case that produces the widest CV. The CV width therefore increases with the panel stiffness. For panels $P_1$–$P_7$ the ranges are $y_{range} = [0.4, 0.5, 0.6, 0.6, 0.7, 0.725, 0.75]\,C$.

The streamwise extent of the CV is set by considering the entrainment of momentum over the sides. Figure 8(a) shows a CV with the inlet and outlet velocity profiles for panel $P_5$ operating at $k = 6.9$, which is operating near its wake resonant frequency. Figure 8(b) shows the product $uv$, which indicates where momentum is entrained into or expelled from the velocity jet ($u$ and $v$ are the streamwise and cross-stream components of velocity, respectively). From plots like this, we set the outlet location of the CV at the boundary between the entraining and expelling regions. This location is fixed for a given panel over the range of tested frequencies at the value that gives the shortest entrainment region. The CV length therefore decreases with the panel stiffness. For panels $P_1$ and $P_2$ the entrainment region extends to $x/C = 1$, for panel $P_3$ it extends to $x/C = 0.6$, for panels $P_4$–$P_6$ it extends to $x/C = 0.5$, and for panel $P_7$ it extends to $x/C = 0.45$.

We now define the entrainment ratio, $\gamma$, as the ratio of the streamwise momentum flux entrained through the sides of the CV to the momentum flux at the inlet, so that

$$\gamma = \frac{\int_{side} uv\ dl}{\int_{in} u^2\ dl}, \tag{6}$$

where the integration is along the perimeter of the rectangular CV. Figure 9 (left) shows the velocity profiles at the inlet and outlet, as well as the side boundaries of the CV (horizontal solid lines) for

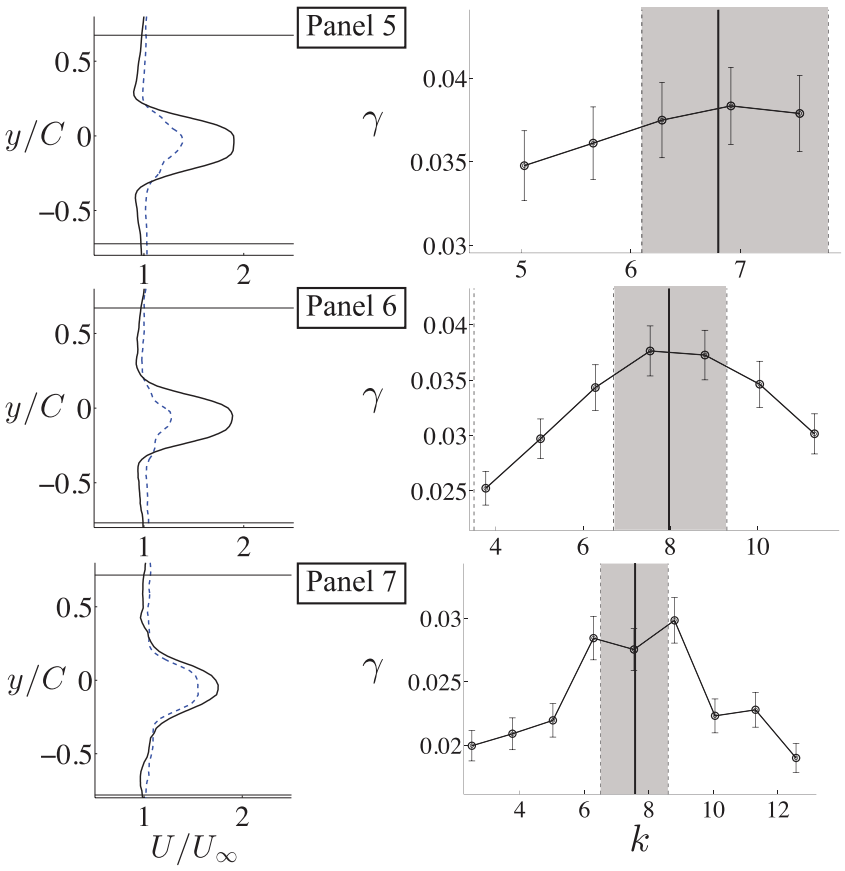


FIG. 10. Data for the least flexible panels $P_5$–$P_7$: (Left) Velocity profiles at $k = 6.3$ for the inlet (dashed profile) and the outlet (solid profile). The sides of the CV are marked with horizontal solid lines. (Right) Entrainment ratio as a function of reduced frequency. The solid line represents the mean values of the wake resonant frequencies while the dashed lines are the minimum and maximum values of the wake resonant frequencies.

panels $P_1$–$P_4$. All of the velocity profiles exhibit enhanced momentum flux at the outlet. Figure 9 (right) shows the calculated entrainment ratio where the uncertainty is estimated from a 3% error in the velocity measurements. Within the uncertainties, all of the wake resonant frequencies are in good agreement with the peaks in the entrainment ratio, with the single exception of the third wake resonant frequency for panel $P_2$. The enhanced entrainment for this case may be underresolved because of the relatively coarse steps in frequency used to obtain the PIV data. Figure 10 shows the velocity profiles and entrainment ratio data for panels $P_5$–$P_7$. Again, there is good agreement between the wake resonant frequencies and the peaks in the entrainment ratio. It appears, therefore, that at a wake resonant frequency the entrainment of momentum into the time-averaged velocity jet is locally maximized, which concurrently leads to a local peak in propulsive efficiency.

## VIII. CONCLUDING REMARKS

This work extends wake resonance theory to include flexible propulsors, and leads to a number of original conclusions. First, it was found that for flexible propulsors each peak in efficiency occurs when the driving frequency of motion is tuned to a wake resonant frequency, not a structural resonant frequency. Second, the panel flexibility that attains global optimally efficient locomotion is the one where a structural resonant frequency is tuned to a wake resonant frequency. Thus, the primary principle to achieve efficient locomotion is to tune the frequency of motion to a wake resonant frequency, while the secondary principle is to tune the structural resonant frequency to a wake resonant frequency. We saw that the tuned flexible panels exhibit a 122%–133% increase in efficiency over the rigid panel, while the untuned flexible panels exhibit an 33%–88% increase in efficiency. All of the flexible panels displayed enhanced efficiency performance over the rigid panel.

The physical mechanism for enhanced efficiency is identified as the maximization of the entrainment of momentum into the velocity jet. The entrained momentum enhances the momentum flux of the jet and leads to higher efficiency. The Strouhal number range of the wake resonant frequencies in this and previous studies ($0.16 \leq St \leq 0.42$) coincides with the Strouhal range of most flying and swimming animals ($0.2 \leq St \leq 0.4$).[35] Hence, we propose a unifying principle in biological locomotion: animals tune to the hydrodynamic resonance of their wakes regardless of whether their propulsors are rigid or flexible. Also, because the frequency of wake resonance is finite, and the frequency of structural resonance of a rigid propulsor is infinite, the global optimally efficient propulsion is guaranteed to occur for flexible propulsors and not rigid ones. Finally, it is concluded that when the panel flexibility is optimally tuned there is a broad spectrum of wake resonant frequencies that make it possible to achieve high efficiency swimming over a wide range of operating conditions.

## ACKNOWLEDGMENTS

These authors would like to thank the generous support provided by the Office of Naval Research under Program Director Dr. Bob Brizzolara, MURI Grant No. N00014-08-1-0642.

## APPENDIX: SENSITIVITY ANALYSIS

The sensitivity of the eigenvalue analysis to uncertainty in the PIV measurements was quantified. Following Moored *et al.*,[10] an ideal velocity profile was analyzed to find its resonant frequency:

$$\frac{U(y/C)}{U_\infty} = 1 + sech^2\left(7\,\frac{y}{C}\right) \quad \text{from } -2 \leq y/C \leq 2. \tag{A1}$$

All dimensional parameters are nondimensionalized by $C = 0.12$ m, $U_\infty = 0.06$ m/s, and the chord-based Reynolds number is $Re = 7171$ based on a kinematic viscosity of $\nu = 1.004 \times 10^{-6}$ m$^2$/s. The resonant frequency was calculated to be $k = 8.09$. Random noise was added to the ideal velocity profile with an amplitude between 1% and 5% of the difference between the peak velocity and the free-stream velocity. This models the uncertainty in the PIV measurements. An example of an ideal

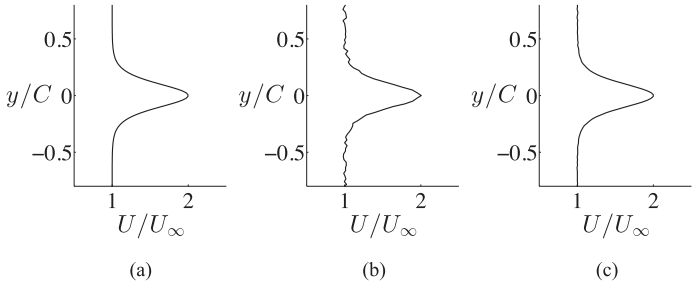


FIG. 11. (a) An ideal velocity profile. (b) A velocity profile with noise added of an amplitude that is 5% of the difference between the peak and free-stream velocities. (c) A velocity profile that is the average of twenty-four randomly generated profiles with 5% noise.

velocity profile and a profile with 5% noise can be found in Figures 11(a) and 11(b). Twenty-four randomly generated noisy velocity profiles were averaged to replicate the averaging that occurs in the experiments over twenty-four oscillation cycles. An example of an averaged 5% noisy profile can be observed in Figure 11(c). After an averaged noisy profile is generated, a moving average filter is included to exactly emulate the processing procedure used on the experimental data. The moving average filter is used to smooth out the second derivative of the velocity profile, $U''(y)$, where the moving average is windowed over a interval that is 1% of the range $-2 \leq y/C \leq 2$. Figure 11(c) has been processed with the moving average filter.

From ten randomly generated, averaged 1% noisy velocity profiles, the uncertainty in the most unstable frequency of the profile was always less than 1% from the exact value while for averaged 5% noisy velocity profiles, the uncertainty was always less than 3.5% from the exact value. Thus, the range of estimated uncertainty in the calculation of the wake resonant frequencies is 1%–3.5% due to a 1%–5% uncertainty in the velocity measurements.

[1] P. A. Dewey, B. M. Boschitsch, K. W. Moored, H. A. Stone, and A. J. Smits, "Scaling laws for the thrust production of flexible pitching panels," J. Fluid Mech. **732**, 29–46 (2013).
[2] D. Barkley, "Linear analysis of the cylinder wake mean flow," Europhys. Lett. **75**(5), 750–756 (2006).
[3] B. Thiria and J. E. Wesfreid, "Stability properties of forced wakes," J. Fluid Mech. **579**, 137–161 (2007).
[4] B. J. McKeon and A. S. Sharma, "A critical-layer framework for turbulent pipe flow," J. Fluid Mech. **658**, 336–382 (2010).
[5] G. V. Lauder, E. G. Drucker *et al.*, "Forces, fishes, and fluids: Hydrodynamic mechanisms of aquatic locomotion," News 411 Physiol. Sci. **17**, 235–240 (2002).
[6] F. E. Fish and G. V. Lauder, "Passive and active flow control by swimming fishes and mammals," Annu. Rev. Fluid Mech. **38**, 193–224 (2006).
[7] T. Schnipper, A. Andersen, and T. Bohr, "Vortex wakes of a flapping foil," J. Fluid Mech. **633**, 411–423 (2009).
[8] M. S. Triantafyllou, G. S. Triantafyllou, and R. Gopalkrishnan, "Wake mechanics for thrust generation in oscillating foils," Phys. Fluids A **3**(12), 2835–2837 (1991).
[9] G. S. Triantafyllou, M. S. Triantafyllou, and M. A. Grosenbaugh, "Optimal thrust development in oscillating foils with application to fish propulsion," J. Fluids Struct. **7**(2), 205–224 (1993).
[10] K. W. Moored, P. A. Dewey, A. J. Smits, and H. Haj-Hariri, "Hydrodynamic wake resonance as an underlying principle of efficient unsteady propulsion," J. Fluid Mech. **708**, 329–348 (2012).
[11] M. Vanella, T. Fitzgerald, S. Preidikman, E. Balaras, and B. Balachandran, "Influence of flexibility on the aerodynamic performance of a hovering wing," J. Exp. Biol. **212**(1), 95–105 (2009).
[12] C.-K. Kang, H. Aono, C. E. S. Cesnik, and W. Shyy, "Effects of flexibility on the aerodynamic performance of flapping wings," J. Fluid Mech. **689**, 32–74 (2011).
[13] B. Yin and H. Luo, "Effect of wing inertia on hovering performance of flexible flapping wings," Phys. Fluids **22**(11), 111902 (2010).
[14] S. Ramananarivo, R. Godoy-Diana, and B. Thiria, "Rather than resonance, flapping wing flyers may play on aerodynamics to improve performance," Proc. Natl. Acad. Sci. U.S.A. **108**(15), 5964–5969 (2011).
[15] S. Michelin and S. G. L. Smith, "Resonance and propulsion performance of a heaving flexible wing," Phys. Fluids **21**(7), 071902 (2009).
[16] S. E. Spagnolie, L. Moret, M. J. Shelley, and J. Zhang, "Surprising behaviors in flapping locomotion with passive pitching," Phys. Fluids **22**(4), 041903 (2010).
[17] S. Alben, C. Witt, T. V. Baker, E. Anderson, and G. V. Lauder, "Dynamics of freely swimming flexible foils," Phys. Fluids **24**(5), 051901 (2012).
[18] H. Masoud and A. Alexeev, "Resonance of flexible flapping wings at low Reynolds number," Phys. Rev. E **81**(5), 056304 (2010).

[19] H. Dai, H. Luo, P. J. S. A. Ferreira de Sousa, and J. F. Doyle, "Thrust performance of a flexible low-aspect-ratio pitching plate," Phys. Fluids **24**(10), 101903 (2012).
[20] P. W. Webb, "Simple physical principles and vertebrate aquatic locomotion," Am. Zoologist **28**(2), 709–725 (1988); available at http://www.jstor.org/stable/3883299.
[21] M. A. Green, C. W. Rowley, and A. J. Smits, "The unsteady three-dimensional wake produced by a trapezoidal pitching panel," J. Fluid Mech. **685**(1), 117–145 (2011).
[22] G. V. Lauder, P. G. A. Madden, J. L. Tangorra, E. Anderson, and T. V. Baker, "Bioinspiration from fish for smart material design and function," Smart Mater. Struct. **20**(9), 094014 (2011).
[23] F. Gosselin, E. de Langre, and B. A. Machado-Almeida, "Drag reduction of flexible plates by reconfiguration," J. Fluid Mech. **650**, 319–341 (2010).
[24] J. M. Jimenéz, "Low reynolds number studies in the wake of a submarine model using particle image velocimetry," Master's thesis, Princeton University, Princeton, NJ, 2002.
[25] A. S. Chan, P. A. Dewey, A. Jameson, C. Liang, and A. J. Smits, "Vortex suppression and drag reduction in the wake of counter-rotating cylinders," J. Fluid Mech. **679**, 343–382 (2011).
[26] P. A. Dewey, A. Carriou, and A. J. Smits, "On the relationship between efficiency and wake structure of a batoid-inspired oscillating fin," J. Fluid Mech. **691**, 245–266 (2012).
[27] G. E. Mattingly and W. O. Criminale, "The stability of an incompressible two-dimensional wake," J. Fluid Mech. **51**(02), 233–272 (1972).
[28] F. R. Gantmacher, *The Theory of Matrices* (Chelsea Publishing Company, New York, NY, 1959), Vol. 1.
[29] T. J. Bridges and P. J. Morris, "Differential eigenvalue problems in which the parameter appears nonlinearly," J. Comput. Phys. **55**(3), 437–460 (1984).
[30] H. Haj-Hariri, "Transformations reducing the order of the parameter in differential eigenvalue problems," J. Comput. Phys. **77**(2), 472–484 (1988).
[31] S. A. Orszag, "Accurate solution of the orr–sommerfeld stability equation," J. Fluid Mech. **50**(04), 689–703 (1971).
[32] J. O. Dabiri, "Optimal vortex formation as a unifying principle in biological propulsion," Annu. Rev. Fluid Mech. **41**, 17–33 (2009).
[33] P. A. Monkewitz, P. Huerre, and J.-M. Chomaz, "Global linear stability analysis of weakly non-parallel shear flows," J. Fluid Mech. **251**, 1–20 (1993).
[34] G. C. Lewin and H. Haj-Hariri, "Modelling thrust generation of a two-dimensional heaving airfoil in a viscous flow," J. Fluid Mech. **492**, 339–362 (2003).
[35] G. K. Taylor, R. L. Nudds, and A. L. R. Thomas, "Flying and swimming animals cruise at a strouhal number tuned for high power efficiency," Nature (London) **425**(6959), 707–711 (2003).
[36] R. P. Clark and A. J. Smits, "Thrust production and wake structure of a batoid-inspired oscillating fin," J. Fluid Mech. **562**, 415–429 (2006).
[37] W. T. Kelvin, "Hydrokinetic solutions and observations," LED Philos. Mag. J. Sci. **42**(281), 362–377 (1871).
[38] H. V. Helmholtz, "On discontinuous movements of fluids," LED Philos. Mag. J. Sci. **36**(244), 337–346 (1868).